AIAA JOURNAL
Vol. 46, No. 4, April 2008

Drag-Breakdown Methods from Wake Measurements

M. Méheut* and D. Bailly†
ONERA, 92322 Châtillon Cedex, France

DOI: 10.2514/1.29051

This paper focuses on drag-extraction methods from flowfield wake surveys. For many years, ONERA has developed an original method which aims at improving the understanding of local flow phenomena. The approach consists in decomposing lift and drag into profile and induced components from wake measurements. The definition of drag allows a phenomenological breakdown of the different drag sources, for which the physical interpretation requires an accurate description of the wake phenomena. It is the aim of this paper to closely analyze these drag sources and to establish an accurate breakdown. In the first section, the analytical definition of profile drag is reviewed. Several formulations commonly found in the literature are compared with determine their physical meaning and limits of applicability. From this analysis, a new drag-breakdown method is proposed and discussed. Computational fluid dynamics simulations are carried out to complete this study and to evaluate the accuracy of the new formulation. The latter is then applied to subsonic and transonic flows from wind-tunnel measurements.

Nomenclature

AR	=	wing aspect ratio
C_D	=	drag coefficient
C_{Di}	=	induced-drag coefficient
C_{Dp}	=	profile drag coefficient
C_{Dv}	=	viscous drag coefficient
D	=	drag
H	=	stagnation enthalpy
M_∞	=	freestream Mach number
$\boldsymbol{n}$	=	unit normal vector
P	=	pressure
P_i	=	stagnation pressure
P_t	=	total pressure, $P + \rho V^2/2$
r	=	gas constant
s	=	specific entropy
S_{ref}	=	reference wing area
T	=	temperature
T_i	=	stagnation temperature
U	=	longitudinal velocity components
U_∞	=	freestream velocity
$\boldsymbol{V}$	=	velocity vector
γ	=	specific heat ratio
δs	=	entropy increment, $(s - s_\infty)$
ζ	=	streamwise vorticity
ρ	=	fluid density
σ	=	longitudinal velocity gradient components
$[\tau]$	=	viscous stress tensor
ϕ	=	velocity potential
ψ	=	crossflow stream function

Subscript

∞	=	undisturbed flow

Received 28 November 2006; revision received 4 July 2007; accepted for publication 10 July 2007.

*Ph.D. Student, Université de Sciences et Technologies de Lille, 59650 Villeneuve d'Ascq.

†Research Scientist, Applied Aerodynamics Department, 29 Avenue de la Division Leclerc.

I. Introduction

NOWADAYS, the design of aircraft is driven primarily by cost reduction as well as by regulation considerations. Indeed, environmental constraints now push for significant reductions in emissions and noise pollution. An answer to the problem can be found either in the improvement of existing aircraft performance or in the development of completely novel configurations. Whatever the solution, the precise evaluation of drag remains a key necessity, not only quantitatively (from a unique force measurement), but also phenomenologically, from a breakdown into viscous, wave, and induced components.

Despite recent progress, the accuracy of computational fluid dynamics (CFD) computations is not yet sufficient to provide a reliable evaluation of the drag components [1,2]. As such, wind-tunnel tests remain the only viable option to a successful prediction. Experimentally, the forces acting on a model are usually determined using balance measurements, which provides very accurate results but no real physical insights.

To overcome this problem, ONERA has developed an original method to determine each drag component using far-field integration. It consists in formulating profile (viscous and wave contributions) and induced-drag components in terms of flow quantities calculated directly inside the wake, downstream of the model.

To guarantee an accurate phenomenological drag expression, an analysis of the drag sources and a study of the different drag formulations are required. Throughout the years, several authors have been working on definitions of profile drag. The first formulations (Jones [3] and Oswatitsch [4]) were established for nonlifting flows. Maskell [5] then developed a general method, but for incompressible flows. ONERA [6,7] and, simultaneously although differently, Kusunose [8] and van Dam [9] recently tackled the compressible problem. These formulations are based on different assumptions and, as such, result in different phenomenological decompositions. This paper aims at evaluating these differences and determining their limits of applicability. Consequently, the formulations are analyzed through a rigorous study of their physical meaning and compared using asymptotic developments to determine differences in their behavior. This study underlines the importance of static pressure and axial velocity fields and shows that none of the previous formulations can provide a reliable experimental drag breakdown for the profile and induced components.

To cope with this problem, an original and general drag-extraction method was developed and applied to three-dimensional CFD computations on several geometries (NACA0012 wing, AS28 wing–body, and generic Falcon) to validate the analysis and to evaluate the accuracy of this new method. In the final comparison, it is applied in subsonic and transonic flows from wind-tunnel measurements.

Eventually, its accuracy was also assessed for subsonic and transonic flows from wind-tunnel surveys.

II. Drag-Breakdown Methods: Analysis and Comparison

A. Far-Field Approach

The far-field approach is based on an integration of the momentum equation inside a closed volume surrounding the model (Fig. 1) and consists in writing drag and lift in terms of wake variables (contrary to the near-field approach, which is an integration over the model surface). In this method, the force acting on a body can be defined as

$$\boldsymbol{F}_a = -\int_{\Sigma_\infty \cup \Sigma_{\text{lat}} \cup \Sigma_1} [\rho(\boldsymbol{V}-\boldsymbol{U}_\infty)(\boldsymbol{V}.\boldsymbol{n}) - [\tau].\boldsymbol{n} + (P-P_\infty)\boldsymbol{n}]\,\mathrm{d}s \tag{1}$$

where ρ, P, P_∞, $\boldsymbol{V}$, $\boldsymbol{U}_\infty$, and $[\tau]$ are the density, the local and upstream static pressures and velocity vectors ($\boldsymbol{V}=(U,v,w)$ and $\boldsymbol{U}_\infty = U_\infty.\boldsymbol{x}$), and the shear stress tensor, respectively. The drag is obtained from the previous equation with a projection of $\boldsymbol{F}_a$ on the upstream flow axis $\boldsymbol{x}$:

$$D = -\int_{\Sigma_\infty \cup \Sigma_{\text{lat}} \cup \Sigma_1} [\rho(U-U_\infty)(\boldsymbol{V}.\boldsymbol{n}) - \boldsymbol{\tau}_x.\boldsymbol{n} + (P-P_\infty)n_x]\,\mathrm{d}s \tag{2}$$

The influence of the viscous vector $\boldsymbol{\tau}_x = [\tau].\boldsymbol{x}$ component is known to be negligible if the surfaces of the control volume are far enough from the body [10]. Moreover, the domain of integration in Eq. (2) can be reduced to the downstream plane Σ_1 using realistic assumptions on Σ_{lat} and Σ_∞. On Σ_∞, the flow conditions are equal to the upstream conditions and Σ_{lat} is defined as parallel to the upstream flow, so that its contribution to drag is zero in free-air and wind-tunnel conditions. Equation (2) can, as a consequence, be rewritten as

$$D = -\int_{\Sigma_1} [\rho(U-U_\infty)(\boldsymbol{V}.\boldsymbol{n}) + (P-P_\infty)n_x]\,\mathrm{d}s \tag{3}$$

Introducing the drag coefficient C_D,

$$C_D = \frac{2D}{\rho_\infty U_\infty^2 S_{\text{ref}}} \tag{4}$$

where S_{ref} and ρ_∞ are the reference surface and the upstream density, and using Eq. (3), we obtain

$$C_D = \frac{2}{S_{\text{ref}}}\int_{\Sigma_1}\left[\frac{\rho}{\rho_\infty}\frac{U}{U_\infty}\left(1-\frac{U}{U_\infty}\right) + \left(\frac{P_\infty - P}{\rho_\infty U_\infty^2}\right)\right]\mathrm{d}s \tag{5}$$

The drag coefficient can also be written in terms of wake variables measured in the wind tunnel:

$$C_D = \frac{2}{S_{\text{ref}}}\int_{\Sigma_1}\left[\frac{T_{i\infty}}{T_i}\frac{P_i}{P_{i\infty}}\Im^{\frac{1}{\gamma-1}}\frac{U}{U_\infty}\left(1-\frac{U}{U_\infty}\right) + \frac{1}{\gamma M_\infty^2}\left(1-\frac{P_i}{P_{i\infty}}\Im^{\frac{\gamma}{\gamma-1}}\right)\right]\mathrm{d}s \tag{6}$$

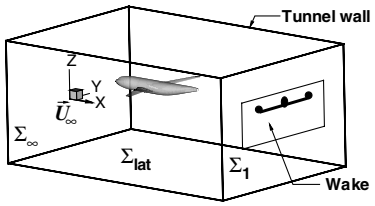

Fig. 1 Control volume.

where M_∞, γ, P_i, $P_{i\infty}$, T_i, and $T_{i\infty}$ are the upstream Mach number; the ratio of specific heats; the local and upstream stagnation pressures and temperatures, respectively; and $\Im$ is defined as

$$\Im = 1 + \frac{\gamma-1}{2}M_\infty^2\left(1-\frac{V^2}{U_\infty^2}\frac{T_{i\infty}}{T_i}\right) \tag{7}$$

Equation (6) allows the determination of the total drag but does not provide a physical drag breakdown. To cope with this deficiency, the different drag sources have to be separated to define formulations for the profile and induced components. To simplify the notation, the term "drag" will refer to the drag coefficient in the remaining of this article.

B. Profile and Induced-Drag Definitions

Many definitions of the profile drag exist in the literature. They can be classified into two categories: those based on nonlifting assumption and those derived for general incompressible or compressible flows.

1. Formulations for Nonlifting Flows

Betz [11], Jones [3], and Oswatitsch [4] established their own formulations for nonlifting and adiabatic flows without vorticity. For the first two, the velocity vector is assumed to be parallel to the upstream flow in the measuring plane Σ_1 ($\boldsymbol{V} = U.\boldsymbol{x}$).

a. Betz Formulation. In 1925, Betz [11] defined the first profile drag formula from Eq. (5):

$$C_{\text{Dp}}^{\text{Betz}} = \frac{2}{S_{\text{ref}}}\int_{\Sigma_1}\left(\frac{P_i}{P_{i\infty}}\right)^{\frac{\gamma-1}{\gamma}}\left(\frac{P}{P_\infty}\right)^{\frac{1}{\gamma}}\sqrt{\frac{1-\left(\frac{P}{P_i}\right)^{\frac{\gamma-1}{\gamma}}}{1-\left(\frac{P_\infty}{P_{i\infty}}\right)^{\frac{\gamma-1}{\gamma}}}} \times\left(1-\sqrt{\frac{1-\left(\frac{P}{P_i}\right)^{\frac{\gamma-1}{\gamma}}}{1-\left(\frac{P_\infty}{P_{i\infty}}\right)^{\frac{\gamma-1}{\gamma}}}} + \frac{\left(\frac{P}{P_i}\right)^{\frac{\gamma-1}{\gamma}}\left(\frac{P_\infty}{P}-1\right)}{\frac{2\gamma}{\gamma-1}\sqrt{1-\left(\frac{P_\infty}{P_{i\infty}}\right)^{\frac{\gamma-1}{\gamma}}}\sqrt{1-\left(\frac{P}{P_i}\right)^{\frac{\gamma-1}{\gamma}}}}\right)\mathrm{d}s \tag{8}$$

To establish this formulation, he considered an adiabatic and irrotational flow, which is rigorous for bidimensional flows. Yet its application to lifting flows implies that some effects, due to the development of the circulation around the body, are attributed to the profile drag, whereas these effects are, in fact, attributable to the trailing vortices and the induced drag. Indeed, Eq. (8) shows a dependence on static pressure variations. Physically, these variations are mostly due to the development of the vorticity field and the trailing vortices downstream of a lifting configuration. Figure 2 underlines this aspect from two Navier–Stokes solutions on a NACA0012 wing for two Mach numbers (0.2 and 0.8) in a wake plane located at one chord downstream of the wing. It presents the static and stagnation pressure distributions downstream of the wing. The static pressure variations are located not only in the viscous and wave wakes, but in the entire downstream plane, unlike the stagnation pressure variations. Consequently, the application of the Betz formulation [11] in a complete flow from wake data cannot provide a reliable evaluation of the profile drag.

b. Jones Formulation. In 1936, Jones [3] developed a new formulation. He used the same assumptions as Betz [11], but he also assumed the existence of a downstream plane Σ_2 located in the far field, in which the static pressure variations are zero ($P_2 = P_\infty \Sigma_2$ is a Trefftz plane). Moreover, the flow between Σ_1 and Σ_2 is assumed to remain isentropic. The profile drag is derived from Eq. (5) in the wake plane by

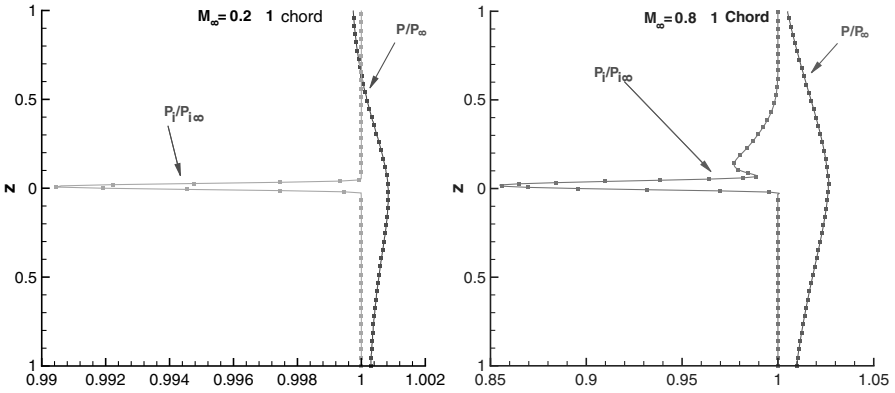

Fig. 2 NACA0012: Navier–Stokes computations ($\alpha = 2.5$ deg); static and stagnation pressures distributions downstream of the wing for $M_\infty = 0.2$ and $M_\infty = 0.8$.

$$C_{\mathrm{Dp}}^{\mathrm{Jones}} = \frac{2}{S_{\mathrm{ref}}} \int_{\mathrm{wake}} \left[\left(\frac{P_i}{P_{i\infty}}\right)^{\frac{\gamma-1}{\gamma}} \left(\frac{P}{P_\infty}\right)^{\frac{1}{\gamma}} \sqrt{\frac{1-\left(\frac{P}{P_i}\right)^{\frac{\gamma-1}{\gamma}}}{1-\left(\frac{P_\infty}{P_{i\infty}}\right)^{\frac{\gamma-1}{\gamma}}}} \times \left(1 - \sqrt{\frac{1-\left(\frac{P_\infty}{P_i}\right)^{\frac{\gamma-1}{\gamma}}}{1-\left(\frac{P_\infty}{P_{i\infty}}\right)^{\frac{\gamma-1}{\gamma}}}} \right) \right] \mathrm{d}s \tag{9}$$

With this new assumption, the domain of integration of Eq. (9) can be reduced to the only wake. Here, the main effects due to the static pressure variations are not taken into account. They are mainly responsible for the induced drag, so that the application of this formulation in a complete flow provides a more reliable breakdown than the Betz [11] formulation, in which these effects are entirely attributed to the profile drag.

However, this new assumption imposes a restriction on the stagnation pressure losses. Indeed, the existence of a downstream Trefftz plane implies that the local stagnation pressure has to remain greater than the upstream static pressure in the entire wake flow. Otherwise, the static pressure cannot reach its upstream value in a downstream plane because of the isentropic flow assumption between Σ_1 and Σ_2. Moreover, in these conditions, the term under the second square root in Eq. (9) becomes negative if $P_i < P_\infty$, and the profile drag cannot be evaluated. Such a condition can be reached downstream of very strong shocks or in the wake of high-lift configurations. As an illustration, Fig. 3 shows a P_i/P_∞ field downstream of a typical high-lift configuration equipped with a slat and a flap.

This condition on the stagnation pressure field can also be reached downstream of strong shocks in transonic flows. Using a theoretical approach, the field of application of the formulation can be determined from a simple normal shock model. From the isentropic flow condition between the upstream plane and the shock and the Rankine–Hugoniot relations, the ratio P_{i2}/P_∞ can be expressed as

$$\frac{P_{i2}}{P_\infty} = \frac{2\gamma M_1^2 - (\gamma-1)}{\gamma+1} \left[\frac{1+\frac{\gamma-1}{2}M_\infty^2}{1+\frac{\gamma-1}{2}M_1^2} \right]^{\frac{\gamma}{\gamma-1}} \times \left[1 + \frac{\gamma-1}{2} \frac{(\gamma-1)M_1^2+2}{2\gamma M_1^2-(\gamma-1)} \right]^{\frac{\gamma}{\gamma-1}} \tag{10}$$

where P_{i2} is the downstream shock stagnation pressure and P_∞ is the upstream pressure. The Jones [3] formulation can be applied only if $P_{i2} > P_\infty$. Figure 4 allows the definition of a criterion on both upstream and far-field Mach numbers to determine the field of application of relation (9). For example, for an upstream Mach number of 0.8, the local Mach number has to reach over 2.15 to violate the assumption underlying the formulation. Such a condition is never intentionally reached around civil aircraft configurations. Yet, for an upstream Mach number of 0.25, the Jones formulation is

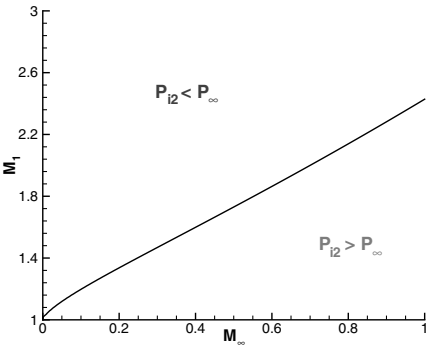

Fig. 4 Conditions of application of the Jones [3] formulation in transonic flows.

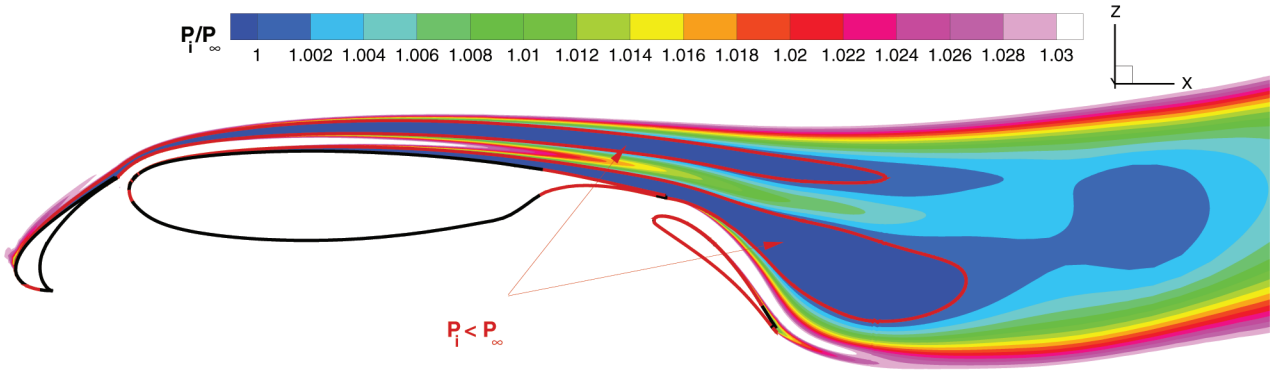

Fig. 3 Navier–Stokes computations ($M_\infty = 0.22$, $\alpha = 25$ deg, and $Re_c = 3.1 \times 10^6$); P_i/P_∞ field.

no longer valid when the local Mach number reaches 1.4. Such a situation can occur on the slat of high-lift configurations at high angles of attack (over 20 deg).

Furthermore, with the Jones [3] formulation, all viscous and wave drag sources and a small part of the static pressure variations are attributed to the profile drag, which is known to be nonphysical.

c. Oswatitsch Formulation. In 1956, Oswatitsch [4] established a new profile drag formulation. The position of the measuring plane is such that only the first-order terms can be considered. The profile drag is defined according to the entropy variations by

$$C_{\mathrm{Dp}}^{\mathrm{Oswatitsch}} = \frac{2}{S_{\mathrm{ref}}} \int_{\mathrm{wake}} \frac{1}{\gamma M_\infty^2} \frac{\rho}{\rho_\infty} \frac{U}{U_\infty} \frac{\Delta s}{r} \, \mathrm{d}s \tag{11}$$

where r is the gas constant and Δs the entropy variations of a fluid particle between the measuring plane and the upstream flow.

To establish this formulation, Oswatitsch [4] defined his control volume so that the second-order terms could be neglected in the profile drag formulation Eq. (11). However, the preceding formulation is not a rigorous first-order asymptotic development in that the density and the axial velocity are affected by the entropy variations. This assumption allows the elimination of the influence of the crossflow velocity, which is responsible for the induced drag, but does not ensure that all the viscous and shock effects are accounted for in the profile drag. Indeed, second-order terms were unjustifiably neglected. As a result, this formulation is not suitable for a reliable evaluation of the profile drag in all flow conditions.

2. *General Formulations for Incompressible or Compressible Flows*

a. Maskell Formulation. Maskell [5], in 1972, established a new drag-breakdown expression, but for incompressible flows. From the total pressure P_t field, he used the artificial velocity U^* as defined by Betz [11]:

$$P_{t\infty} = P + \frac{\rho}{2}(U^{*2} + v^2 + w^2) \tag{12}$$

He defined a blockage velocity u_b by

$$u_b = \frac{1}{2S_T} \int_{\mathrm{wake}} (U^* - U) \, \mathrm{d}s \tag{13}$$

where S_T is the wind-tunnel cross section. According to Maskell [5], this velocity can be interpreted as a correction of the confinement effect. The correction is introduced by replacing the upstream velocity U_∞ with the effective velocity $U_e = U_\infty + u_b$. Consequently, the profile drag is defined by

$$C_{\mathrm{Dp}}^{\mathrm{Maskell}} = \frac{2}{S_{\mathrm{ref}}} \int_{\mathrm{wake}} \left(\frac{P_{t\infty} - P_t}{\rho_\infty U_\infty^2} \right) \mathrm{d}s + \frac{1}{S_{\mathrm{ref}}} \frac{\rho}{\rho_\infty} \int_{\mathrm{wake}} \left(\frac{U^* - U}{U_\infty} \right) \left(\frac{U^* + U - 2(U_\infty + u_b)}{U_\infty} \right) \mathrm{d}s \tag{14}$$

and the induced drag is defined by

$$C_{\mathrm{Di}} = \frac{1}{S_{\mathrm{ref}}} \frac{\rho}{\rho_\infty} \int_{\Sigma_1} \left(\frac{v^2 + w^2}{U_\infty^2} \right) \mathrm{d}s \tag{15}$$

To reduce the integral of the induced-drag expression to the wake, Maskell [5] introduced the idea of defining scalar functions ϕ and ψ for the cross-sectional velocities v and w; ϕ and ψ are related to the trailing vorticity ζ and the velocity gradient σ through Poisson equations $\Delta\psi = -\zeta$ and $\Delta\phi = \sigma$; and ζ is assumed to be zero outside the wake. Maskell obtained

$$C_{\mathrm{Di}}^{\mathrm{Maskell}} = \frac{1}{S_{\mathrm{ref}}} \frac{\rho}{\rho_\infty} \int_{\mathrm{wake}} \frac{\psi\zeta}{U_\infty^2} \, \mathrm{d}s - \frac{1}{S_{\mathrm{ref}}} \frac{\rho}{\rho_\infty} \int_{\Sigma_1} \frac{\phi\sigma}{U_\infty^2} \, \mathrm{d}s \tag{16}$$

However, this formulation is not only appropriate for incompressible flows. Betz's [11] definition of U^* is consistent with and intended to be used in combination with the Trefftz-plane assumptions. But its use implied that the wake-survey plane must be a Trefftz plane, which is a strong limitation, especially if the wake-survey plane is not so far behind the model. Its application to compressible flows cannot guarantee a reliable evaluation of the drag components. Indeed, Maskell [5] expressed the profile drag according to the total pressure variations. These variations are identical to the stagnation pressure variations in incompressible flows, but not in compressible flows. Figure 5 shows the total, stagnation, and static pressure distributions downstream of a NACA0012 wing for two Mach numbers (0.2 and 0.8). For the lower Mach number, the difference between both pressures is negligible, whereas for the higher Mach number, this difference is relatively important. This behavior explains why the Maskell profile drag formulation cannot be applied to compressible flows. Moreover, the artificial velocity U^* is defined to isolate the axial velocity variations due to viscous and wave effects and it is equal to the axial velocity outside the wake. Figure 6 shows the total and artificial axial velocities distributions downstream of the NACA0012 wing for 2 M numbers. This figure highlights that this definition of the artificial velocity provides a reliable breakdown of this velocity component for incompressible flows, whereas for compressible flows, this breakdown is not able to provide a reliable solution.

The work carried out by Maskell [5] on the induced-drag formulation provides very interesting results. Indeed, the crossflow velocity is related to the trailing vorticity and the velocity gradient. To establish his relation, he did not use the incompressible assumption, so that it can be applied to compressible problems. The main advantage of this formulation comes from the fact that the

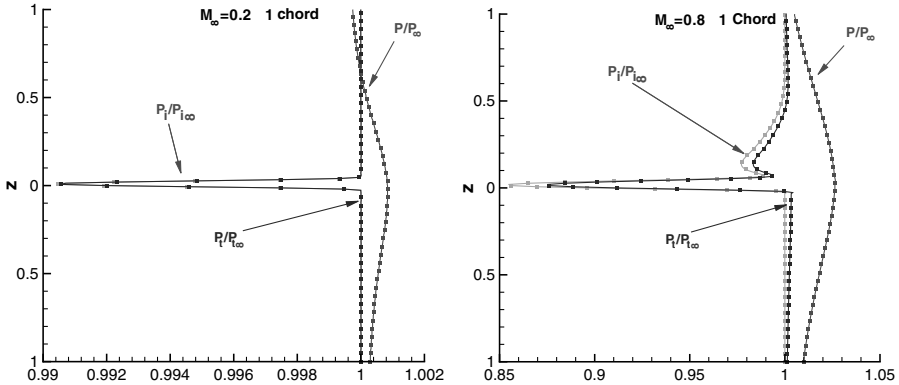

Fig. 5 NACA0012: Navier–Stokes computations ($\alpha = 2.5\,\mathrm{deg}$); total, stagnation, and static pressure distributions downstream of the wing for $M_\infty = 0.2$ and $M_\infty = 0.8$.

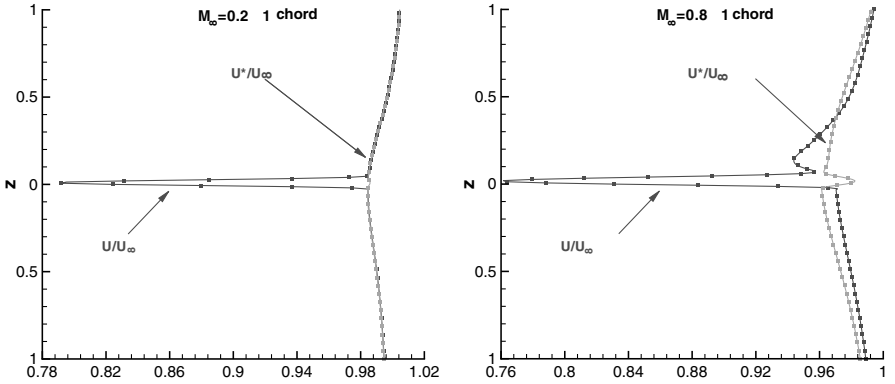

Fig. 6 NACA0012: Navier–Stokes computations ($\alpha = 2.5$ deg); artificial and total axial velocity distributions downstream of the wing for $M_\infty = 0.2$ and $M_\infty = 0.8$.

integration domain of Eq. (16) is reduced to the wake for the vorticity term. On civil aircraft configurations, the velocity gradient term is negligible in comparison with the vorticity gradient term, and so the Maskell induced-drag formulation provides a quite reliable evaluation of the induced drag from wake data. However, for a rigorous drag breakdown, an accurate analysis of this velocity gradient term has to be carried out.

To summarize, this formulation cannot be applied to all configurations for a reliable drag breakdown but provides very useful relations to reduce the domain of integration for induced-drag component to the sole wake.

b. Van der Vooren Formulation. To deal with three-dimensional compressible flows, van der Vooren et al. [2,12] established, in 1990, a new expression of the profile drag, assuming the existence of a Trefftz plane and isentropic and adiabatic flow between the wake-survey and Trefftz planes. So the profile drag becomes

$$C_{\mathrm{Dp}}^{\mathrm{VDV}} = -\frac{2}{S_{\mathrm{ref}}} \int_{\mathrm{wake}} \frac{\rho}{\rho_\infty} \frac{U}{U_\infty} \frac{\Delta \bar{u}}{U_\infty} \, \mathrm{d}s \tag{17}$$

where $\Delta \bar{u}$ depends on the gas constant r and the entropy and stagnation enthalpy variations Δs and ΔH_i:

$$\Delta \bar{u} = U_\infty \left(\sqrt{1 - \frac{2}{(\gamma - 1) M_\infty^2} \left(e^{\frac{\gamma - 1}{\gamma} \frac{\Delta s}{r}} - 1 \right) + \frac{2 \Delta H_i}{U_\infty^2}} - 1 \right) \tag{18}$$

This formulation is applied to three-dimensional compressible flows, and the induced drag is defined by the difference between the total and the profile drag:

$$C_{\mathrm{Di}}^{\mathrm{VDV}} = -\frac{2}{S_{\mathrm{ref}}} \int_{\Sigma_1} \left[\frac{\rho}{\rho_\infty} \frac{U - U_\infty - \Delta \bar{u}}{U_\infty} \frac{U}{U_\infty} + \frac{P - P_\infty}{\rho_\infty U_\infty^2} \right] \mathrm{d}s \tag{19}$$

However, the consequences are identical to Jones's [3] description concerning the restriction on the stagnation pressure field [indeed, in the entire flow, this stagnation pressure has to remain higher than the upstream static pressure; otherwise, the term under the square root in Eq. (18) becomes negative and the contribution to the drag of this point cannot be evaluated].

From the phenomenological point of view, $\Delta \bar{u}$ represents the axial velocity variations due to the viscous and wave effects. This formulation introduces the concept, as did Maskell's [5] with the artificial velocity, of breaking down the axial velocity variations into two components. The first component, $\Delta \bar{u}$, is due to the viscous and wave effects and is zero outside the wake, and the second component, Δu^* ($= \Delta u - \Delta \bar{u}$), is a consequence of the development of the vorticity field and is not affected by the presence of the viscous and wave wakes. Figure 7 shows the breakdown carried out by van der Vooren et al. [2,12] on a NACA0012 wing for two Mach numbers. This figure highlights the good behavior of this formulation, because Δu^* is weakly affected by the crossing of the viscous and wave wakes and is equal to Δu outside the wake.

The second step of this development is the definition of the induced drag, which is simply defined as the difference between the total and the profile drag components [Eq. (19)]. This definition guarantees a complete drag balance, but its domain of integration cannot be reduced to the wake. In conclusion, the van der Vooren et al. [2,12] formulation provides a reliable drag breakdown with a restriction on the stagnation pressure field. Moreover, the formulation for the induced drag cannot be applied from wake measurements only.

c. Kusunose Formulation. To cope with all three-dimensional compressible flows and to obtain a formulation with a domain of integration reduced to the wake, Kusunose [8] established a new drag-breakdown method based on the small-perturbation assumption in 1999. At the same time, a similar formulation was developed by van Dam [9].

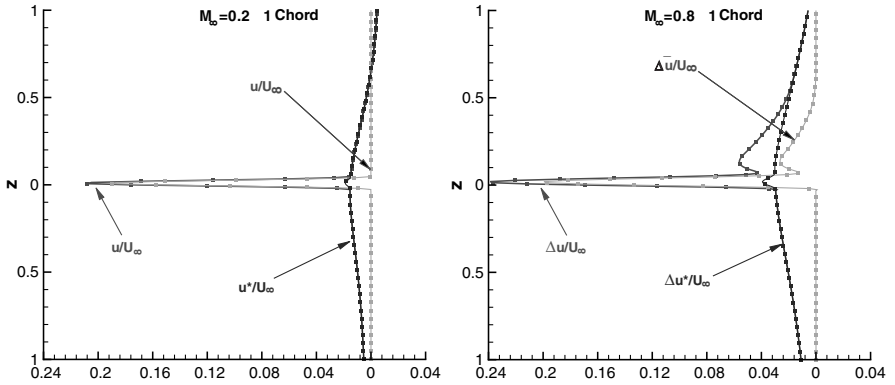

Fig. 7 NACA0012: Navier–Stokes computations ($\alpha = 2.5$ deg); axial velocity breakdown downstream of the wing for $M_\infty = 0.2$ and $M_\infty = 0.8$ with the van der Vooren et al. [2,12] formulation.

Let us assume that downstream states differ only slightly from their upstream values:

$$\begin{cases} U = U_\infty + \delta u \\ \rho = \rho_\infty + \delta\rho \\ P = P_\infty + \delta P \end{cases} \tag{20}$$

with $\delta P/P_\infty, \delta\rho/\rho_\infty$, and $\delta u/U_\infty \ll 1$. To limit the integration to the wake, the density and static pressure are written in terms of entropy and stagnation enthalpy variations δs and δH_i. A second-order asymptotic development of the drag expression (5) leads to a new formulation:

$$C_D^{\text{Kusunose}} = \frac{2}{S_{\text{ref}}}\int_{\text{wake}}\left[\frac{1}{\gamma M_\infty^2}\frac{\delta s}{r} - \frac{\delta H_i}{U_\infty^2} - \frac{1}{2}\frac{1}{\gamma M_\infty^2}\left(\frac{\delta s}{r}\right)^2 + \frac{\delta H_i}{U_\infty^2}\left(\frac{\delta s}{r} - \frac{M_\infty^2}{2}\frac{\delta H_i}{U_\infty^2}\right)\right]\mathrm{d}s + \frac{1}{S_{\text{ref}}}\int_{\Sigma_1}\left[\left(\frac{v^2+w^2}{U_\infty^2}\right) - (1-M_\infty^2)\left(\frac{\delta u}{U_\infty}\right)^2\right]\mathrm{d}s + \mathcal{O}(\delta^3) \tag{21}$$

$\mathcal{O}(\delta^3)$ denotes the third- and higher-order terms. Unfortunately, the second term is not a wake integral. To overcome this problem, Kusunose [8] used the findings of Maskell [5] to relate the cross-sectional velocities with the trailing vorticity ζ and the velocity gradient σ. In 1996, Cummings et al. [13] showed that the second term in Eq. (16) can be expressed according to the axial velocity variations δu:

$$\int_{\Sigma_1}\left(1-M_\infty^2\right)\left(\frac{\delta u}{U_\infty}\right)^2\mathrm{d}s = -\int_{\Sigma_1}\frac{\phi\sigma}{U_\infty^2}\,\mathrm{d}s + \mathcal{O}(\delta^3) \tag{22}$$

with this relation, the second integral of Eq. (21) is reduced to the wake and the Kusunose [8] induced-drag component becomes

$$C_{\text{Di}}^{\text{Kusunose}} = \frac{1}{S_{\text{ref}}}\int_{\text{wake}}\frac{\psi\zeta}{U_\infty^2}\,\mathrm{d}s \tag{23}$$

To complete the drag breakdown, Kusunose [8] defined the other terms in the profile drag:

$$C_{\text{Dp}}^{\text{Kusunose}} = \frac{2}{S_{\text{ref}}}\int_{\text{wake}}\left[\frac{1}{\gamma M_\infty^2}\frac{\delta s}{r} - \frac{\delta H_i}{U_\infty^2} - \frac{1}{2}\frac{1}{\gamma M_\infty^2}\left(\frac{\delta s}{r}\right)^2 + \frac{\delta H_i}{U_\infty^2}\left(\frac{\delta s}{r} - \frac{M_\infty^2}{2}\frac{\delta H_i}{U_\infty^2}\right)\right]\mathrm{d}s + \mathcal{O}(\delta^3) \tag{24}$$

This formulation is based on an asymptotic development of the drag expression with respect to the entropy, enthalpy, and velocity variations. The domain of integration for the profile and induced-drag formulations is reduced to the wake only. The use of the small-disturbance assumption is arguable, because in some cases, the stagnation pressure and velocity variations are not small in comparison with the upstream conditions. For example, in high-lift configurations, the crossflow velocity is very strong and can almost be equal to the upstream value; in transonic flows, stagnation pressure variations can reach up to 20%. The influence of this assumption on the total drag imbalance was analyzed on these two configurations. The results show that for high-lift configurations, the influence on the total drag is negligible: about 0.1%. For transonic configurations, the influence is more important and can reach up to 3% locally, but the influence on the total drag remains quite small: about 0.6% in a wake plane located at one chord downstream of the model. For all configurations, the small-perturbation assumption is therefore legitimate even if, in transonic conditions, it could be responsible for an error higher than one drag count (dc), or two to three, at worst.

From the phenomenological point of view, Kusunose [8] attributed the entropy and enthalpy variations to the profile drag, which is physically correct. However, the second-order axial velocity variations are attributed to the profile drag, whereas they are attributable to both drag components. To reduce the domain of integration of the induced-drag expression to the wake, Kusunose used the work of Cummings et al. [13] to relate the velocity gradient term of the Maskell [5] equation with the second-order axial velocity term. Cummings et al. [13] demonstrated this relation for an isentropic and isenthalpic flow, whereas Kusunose [8] used it on a complete flow. Physically, the axial velocity variations are strongly affected by the viscous and wave wakes. Consequently, the Cummings et al. [13] relation cannot be applied when considering the total axial velocity variations. In this way, the Kusunose [8] formulation neglects the influence of the axial velocity variations inside the wake and, as such, does not provide a complete drag balance.

d. ONERA Formulations. Simultaneously with Kusunose [8], another method was developed at ONERA [6,7] to determine both drag components from flowfield wake surveys. It is a three-dimensional compressible method based on the small-perturbation assumption. Again, we assume that the downstream states differ only slightly from those upstream:

$$\begin{cases} P_i = P_{i\infty}(1+\delta P_i) \\ T_i = T_{i\infty}(1+\delta T_i) \\ \boldsymbol{V} = U_\infty((1+\delta u)\boldsymbol{i} + \delta v\boldsymbol{j} + \delta w\boldsymbol{k}) \end{cases} \tag{25}$$

with $\delta P_i, \delta T_i, \delta u, \delta v$, and $\delta w \ll 1$. From a second-order asymptotic development of the drag expression (6) and Eq. (16), the drag becomes

$$C_D = \frac{1}{S_{\text{ref}}}\int_{\text{wake}}\left[-\frac{2}{\gamma M_\infty^2}\delta P_i - \delta T_i + \left(1-\frac{M_\infty^2}{4}\right)\delta T_i^2 - \delta P_i\delta T_i\right]\mathrm{d}s + \frac{1}{S_{\text{ref}}}\int_{\text{wake}}\frac{\psi\zeta}{U_\infty^2}\,\mathrm{d}s - \frac{1}{S_{\text{ref}}}\int_{\Sigma_1}\left[\left(1-M_\infty^2\right)\delta u^2 + \frac{\phi\sigma}{U_\infty^2}\right]\mathrm{d}s + \mathcal{O}(\delta^3) \tag{26}$$

where $\mathcal{O}(\delta^3)$ denotes the third- and higher-order terms. Physically, the velocity gradient term is assumed negligible and the δu^2 term cannot be reduced to a wake integral. In Eq. (26), the drag breakdown appears clearly, except for the contribution of the δu^2 term. Consequently, two definitions of the profile drag are possible:

$$C_{\text{Dp}}^{\text{ONERA1}} = \frac{1}{S_{\text{ref}}}\int_{\text{wake}}\left[-\frac{2}{\gamma M_\infty^2}\delta P_i - \delta T_i + \left(1-\frac{M_\infty^2}{4}\right)\delta T_i^2 - \delta P_i\delta T_i\right]\mathrm{d}s + \mathcal{O}(\delta^3) \tag{27}$$

$$C_{\text{Dp}}^{\text{ONERA2}} = \frac{1}{S_{\text{ref}}}\int_{\text{wake}}\left[-\frac{2}{\gamma M_\infty^2}\delta P_i - \delta T_i + \left(1-\frac{M_\infty^2}{4}\right)\delta T_i^2 - \delta P_i\delta T_i\right]\mathrm{d}s - \frac{1}{S_{\text{ref}}}\int_{\Sigma_1}\left(1-M_\infty^2\right)\delta u^2\,\mathrm{d}s + \mathcal{O}(\delta^3) \tag{28}$$

These formulations were developed contemporaneously with Kusunose [8] and are also based on the small-disturbance assumption. Its influence on the drag is identical to the previous case. From the physical point of view, the ONERA formulations provide a complete drag balance, but they do not allow a reliable drag breakdown. Indeed, the second-order axial velocity term is attributed to either the profile or to the induced drag, whereas these velocity variations are attributable to both drag components. The second drawback of these formulations is that their domain of integration cannot be reduced to the wake, which prevents a reliable evaluation of the drag from wake measurements. However, these two formulations underline a key point for an accurate drag

decomposition, which is the breakdown of the axial velocity component.

This analysis shows that all these formulations provide different drag breakdowns and have different physical meanings. To compare them, a second-order asymptotic development of each formulation was carried out and is presented in the following section.

C. Asymptotic Developments of the Profile Drag Formulations

This comparison from asymptotic developments assumes that the small-disturbance assumption does not affect the physical meaning of each expression. It is a reliable assumption in the entire wake, except in some points downstream of the configuration. The profile drag is very slightly affected by these considerations, and the comparison between the asymptotic developments provides a first overview of the differences. The formulations are expressed in terms of stagnation pressure, temperature, and velocity fields, as are the ONERA formulations.

Betz [11] formulation:

$$C_{\mathrm{Dp}}^{\mathrm{Betz}} = \frac{1}{S_{\mathrm{ref}}}\int_{\mathrm{wake}}\left[-\frac{2}{\gamma M_\infty^2}\delta P_i + \frac{1}{4}\left(1-M_\infty^2\right)\delta T_i^2 + \left(1-M_\infty^2\right)\delta T_i \delta u\right]\mathrm{d}s - \frac{1}{S_{\mathrm{ref}}}\int_{\Sigma_1}\left(1-M_\infty^2\right)\delta u^2\,\mathrm{d}s + \mathcal{O}(\delta^3) \tag{29}$$

Jones [3] formulation:

$$C_{\mathrm{Dp}}^{\mathrm{Jones}} = \frac{1}{S_{\mathrm{ref}}}\int_{\mathrm{wake}}\left[-\frac{2}{\gamma M_\infty^2}\delta P_i + \frac{1-M_\infty^2}{\gamma^2 M_\infty^4}\delta P_i^2 + \frac{1-M_\infty^2}{\gamma M_\infty^2}\delta P_i \delta T_i - \frac{2\left(1-M_\infty^2\right)}{\gamma M_\infty^2}\delta P_i \delta u\right]\mathrm{d}s + \mathcal{O}(\delta^3) \tag{30}$$

Oswatitsch [4] formulation:

$$C_{\mathrm{Dp}}^{\mathrm{Oswatitsch}} = \frac{1}{S_{\mathrm{ref}}}\int_{\mathrm{wake}}\left[-\frac{2}{\gamma M_\infty^2}\delta P_i - \frac{2}{(\gamma-1)M_\infty^2}\delta T_i - \frac{1}{\gamma M_\infty^2}\delta P_i^2 - \frac{3-M_\infty^2}{(\gamma-1)M_\infty^2}\delta T_i^2 + \frac{2}{\gamma M_\infty^2}\left(\frac{2\gamma-1}{\gamma-1} - \frac{M_\infty^2}{2}\right)\delta P_i \delta T_i + \frac{2\left(1-M_\infty^2\right)}{(\gamma-1)M_\infty^2}\delta T_i \delta u - \frac{2\left(1-M_\infty^2\right)}{\gamma M_\infty^2}\delta P_i \delta u\right]\mathrm{d}s + \mathcal{O}(\delta^3) \tag{31}$$

Maskell [5] formulation:

$$C_{\mathrm{Dp}}^{\mathrm{Maskell}} = \frac{1}{S_{\mathrm{ref}}}\int_{\mathrm{wake}}\left[-\left(1+\frac{2}{\gamma M_\infty^2}\right)\delta P_i - \frac{M_\infty^2}{2}\delta T_i + M_\infty^2 \delta u - \frac{M_\infty^2}{2}\left(\frac{3}{2} - \frac{2-\gamma}{4}M_\infty^2\right)\delta T_i^2 - \left(1 - \frac{3}{2}M_\infty^2 - \frac{2-\gamma}{2}M_\infty^4\right)\delta u^2 - \frac{M_\infty^2}{2}\delta P_i \delta T_i + M_\infty^2 \delta P_i \delta u - M_\infty^2\left(2 - \frac{2-\gamma}{2}M_\infty^2\right)\delta T_i \delta u + \frac{M_\infty^2}{2}\left(\delta v^2 + \delta w^2\right)\right]\mathrm{d}s + \mathcal{O}(\delta^3) \tag{32}$$

Van der Vooren et al. [2,12] formulation:

$$C_{\mathrm{Dp}}^{\mathrm{vdv}} = \frac{1}{S_{\mathrm{ref}}}\int_{\mathrm{wake}}\left[-\frac{2}{\gamma M_\infty^2}\delta P_i - \delta T_i + \frac{1-M_\infty^2}{\gamma^2 M_\infty^4}\delta P_i^2 + \frac{5-2M_\infty^2}{4}\delta T_i^2 + \frac{1-(\gamma+1)M_\infty^2}{\gamma M_\infty^2}\delta P_i \delta T_i - \frac{2\left(1-M_\infty^2\right)}{\gamma M_\infty^2}\delta P_i \delta u - \left(1-M_\infty^2\right)\delta T_i \delta u\right]\mathrm{d}s + \mathcal{O}(\delta^3) \tag{33}$$

Kusunose [8] and ONERA1 formulations:

$$C_{\mathrm{Dp}}^{\mathrm{Kusunose}} = C_{\mathrm{Dp}}^{\mathrm{ONERA1}} = \frac{1}{S_{\mathrm{ref}}}\int_{\mathrm{wake}}\left[-\frac{2}{\gamma M_\infty^2}\delta P_i - \delta T_i + \left(1-\frac{M_\infty^2}{4}\right)\delta T_i^2 - \delta P_i \delta T_i\right]\mathrm{d}s + \mathcal{O}(\delta^3) \tag{34}$$

ONERA2 formulation:

$$C_{\mathrm{Dp}}^{\mathrm{ONERA2}} = \frac{1}{S_{\mathrm{ref}}}\int_{\mathrm{wake}}\left[-\frac{2}{\gamma M_\infty^2}\delta P_i - \delta T_i + \left(1-\frac{M_\infty^2}{4}\right)\delta T_i^2 - \delta P_i \delta T_i\right]\mathrm{d}s - \frac{1}{S_{\mathrm{ref}}}\int_{\Sigma_1}\left(1-M_\infty^2\right)\delta u^2\,\mathrm{d}s + \mathcal{O}(\delta^3) \tag{35}$$

In adiabatic flows ($\delta T_i = 0$), all the formulations are identical to the first order (δP_i term), except for the Maskell [5] method, which has additional constraints due to the incompressibility assumption. However, for incompressible flows ($M_\infty \to 0$), Maskell's method converges toward the same asymptotic development as the other formulations. For the second order, the formulations are different. The second-order axial velocity term can be absent (Kusunose [8] and ONERA1), expressed according to δu^2 (Betz [11] and ONERA2) or according to δu^2 and $\delta u \delta P_i$ (Jones [3], Oswatitsch [4], and van der Vooren et al. [2,12]).

Moreover, the formulations from Betz [11] and ONERA2 are identical to the second order, which shows that taking into account the static pressure variations or the axial velocity variations due to the crossflow leads to the same result in complex flows. Indeed, in the Betz formulation, the viscous and wave effects and the static pressure variations are considered, whereas in the ONERA2 case, all the axial velocity and stagnation pressure variations are taken into account. The Kusunose [8] formulation is equivalent to the ONERA1 expression, because both neglect the second-order axial velocity variations in the profile drag. The Jones [3] and van der Vooren et al. [2,12] expressions are equivalent, because they are based on very close assumptions.

With the definition of $\Delta\bar{u}$ in the van der Vooren et al. [2,12] formulation (18), the axial velocity variations are broken down into two components. This approach allows a more accurate phenomenological breakdown of the drag sources. However, this formulation is limited in terms of stagnation pressure losses and cannot be applied to all flow conditions. To overcome this problem while conserving this accurate drag breakdown, the following section aims at developing a new method to evaluate both components of the axial velocity variations without restriction on the flowfield.

III. New Drag-Extraction Method

A. Axial Velocity Breakdown

To determine these axial velocity components, the flow is assumed to be adiabatic and isentropic without stagnation pressure and temperature variations. This assumption allows the evaluation of the first component δu^*, due to the development of the crossflow. In these conditions, the static pressure P^* and the axial velocity U^* are defined by the following expression:

$$\begin{cases} P^* = P(P_i = P_{i\infty}, T_i = T_{i\infty}) \\ U^* = U(P_i = P_{i\infty}, T_i = T_{i\infty}) \end{cases} \tag{36}$$

From the isentropic relations, the static pressure can be expressed in terms of velocity components:

$$\frac{P^*}{P_\infty} = \left(1 + \frac{\gamma-1}{2}M_\infty^2\left(1 - \frac{U^{*2}+v^2+w^2}{U_\infty^2}\right)\right)^{\frac{\gamma}{\gamma-1}} \tag{37}$$

The axial velocity is

$$\frac{U^*}{U_\infty} = \sqrt{1 - \frac{2}{(\gamma-1)M_\infty^2}\left(\left(\frac{P^*}{P_\infty}\right)^{\frac{\gamma-1}{\gamma}} - 1\right) - \frac{v^2+w^2}{U_\infty^2}} \tag{38}$$

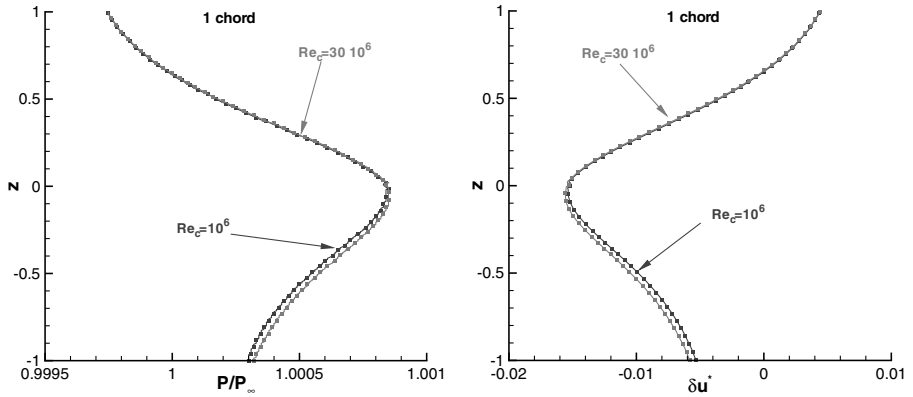

Fig. 8 NACA0012: Navier–Stokes computations ($\alpha = 2.5\,\mathrm{deg}$); static pressure and axial velocity variation distributions downstream of the configuration for two Reynolds numbers (10^6 and 30×10^6).

In the second part, the stagnation pressure and temperature variations are not assumed to be zero. From Eq. (25), both axial velocity variations are defined by

$$\begin{cases} U^* = U_\infty(1 + \delta u^*) \\ \delta\bar{u} = \delta u - \delta u^* \\ U = U^* + \delta\bar{u}U_\infty \end{cases} \tag{39}$$

In three-dimensional compressible flows, the static pressure variations are not really affected by viscous and wave effects in a wake plane located in the far field. Consequently, the static pressure field P^* can be considered equivalent to the static pressure field P in the viscous flow. As a result, the component δu^* of the axial velocity variations can be defined:

$$\delta u^* = \sqrt{1 - \frac{2}{(\gamma-1)M_\infty^2}\left(\left(\frac{P}{P_\infty}\right)^{\frac{\gamma-1}{\gamma}} - 1\right) - \frac{v^2+w^2}{U_\infty^2}} - 1 \tag{40}$$

To evaluate the reliability of this assumption on the pressure field, the influence of Reynolds number on these static pressure variations can be discussed. This number has a very important influence on the viscous effects, but does not affect the other physical phenomena much. It turns out that the static pressure variations and the first axial velocity variations component δu^* have to be practically independent on Reynolds number, as seen in Fig. 8.

From the isentropic relations, the static pressure can be expressed according to $\Im$ and the stagnation pressure field:

$$\frac{P}{P_\infty} = \frac{P_i}{P_{i\infty}}\Im^{\frac{\gamma}{\gamma-1}} \tag{41}$$

where $\Im$ is defined in Eq. (7). The axial velocity variation expression (40) becomes

$$\delta u^* = \sqrt{1 - \frac{2}{(\gamma-1)M_\infty^2}\left(\left(\frac{P_i}{P_{i\infty}}\right)^{\frac{\gamma-1}{\gamma}}\Im - 1\right) - \frac{v^2+w^2}{U_\infty^2}} - 1 \tag{42}$$

The second axial velocity component variation $\delta\bar{u}$ is due to viscous and wave effects and is defined by

$$\delta\bar{u} = \delta u + 1 - \sqrt{1 - \frac{2}{(\gamma-1)M_\infty^2}\left(\left(\frac{P_i}{P_{i\infty}}\right)^{\frac{\gamma-1}{\gamma}}\Im - 1\right) - \frac{v^2+w^2}{U_\infty^2}} \tag{43}$$

This definition guarantees that $\delta\bar{u}$ is zero outside the wake and that the breakdown can be carried out in all configurations without restriction on the flowfield, because it can be shown that

$$1 - \frac{2}{(\gamma-1)M_\infty^2}\left(\left(\frac{P_i}{P_{i\infty}}\right)^{\frac{\gamma-1}{\gamma}}\Im - 1\right) - \frac{v^2+w^2}{U_\infty^2} \geq \frac{U^2}{U_\infty^2} \geq 0 \tag{44}$$

Figure 9 displays the axial velocity breakdown downstream of the NACA0012 wing with this new formulation. The results are compared with those of the van der Vooren et al. [2,12] method for two Mach numbers (0.2 and 0.8). The ONERA formulation provides a more continuous distribution of the δu^* component throughout the wake, especially downstream of the shock in the transonic configuration.

Nevertheless, both formulations provide very close results. With the van der Vooren et al. [2,12] formulation, the $\delta\bar{u}$ component is defined from a flow without static pressure variations and generalized to three-dimensional compressible flows. In this way, the static pressure variations are related to the first component of the axial velocity variations, δu^*, exactly as in the ONERA definition. However, the latter has a great advantage: the stagnation pressure losses are not limited to the wake. To carry out the phenomenological

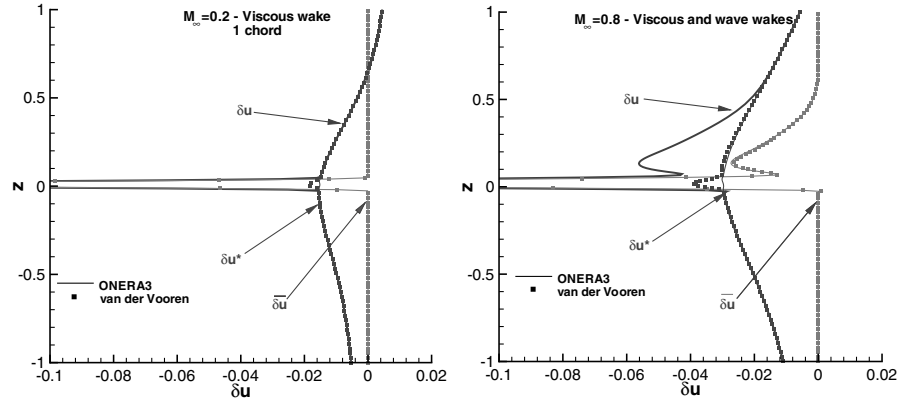

Fig. 9 NACA0012: Navier–Stokes computations ($\alpha = 2.5\,\mathrm{deg}$); axial velocity breakdown downstream of the wing for $M_\infty = 0.2$ and $M_\infty = 0.8$ with the van der Vooren et al. [2,12] and the ONERA3 formulations.

drag breakdown, this definition has to be implemented in drag equation (26).

B. Profile and Induced-Drag Components

The previous axial velocity breakdown is introduced in Eq. (26) and the drag becomes

$$C_D = \frac{1}{S_{\text{ref}}}\int_{\text{wake}}\left[-\frac{2}{\gamma M_\infty^2}\delta P_i - \delta T_i + \left(1-\frac{M_\infty^2}{4}\right)\delta T_i^2 - \delta P_i \delta T_i + \frac{\psi\zeta}{U_\infty^2}\right]\mathrm{d}s - \frac{1}{S_{\text{ref}}}\int_{\Sigma_1}\left[(1-M_\infty^2)(\delta u^* + \delta\bar{u})^2 + \frac{\phi\sigma}{U_\infty^2}\right]\mathrm{d}s + \mathcal{O}(\delta^3) \tag{45}$$

where $\delta\bar{u}$ is zero outside the wake, and the second integral can be partially reduced to the wake:

$$C_D = \frac{1}{S_{\text{ref}}}\int_{\text{wake}}\left[-\frac{2}{\gamma M_\infty^2}\delta P_i - \delta T_i + \left(1-\frac{M_\infty^2}{4}\right)\delta T_i^2 - \delta P_i \delta T_i - \left(1-M_\infty^2\right)(\delta\bar{u}^2 + 2\delta u^*\delta\bar{u}) + \frac{\psi\zeta}{U_\infty^2}\right]\mathrm{d}s - \frac{1}{S_{\text{ref}}}\int_{\Sigma_1}\left[\left(1-M_\infty^2\right)\delta u^{*2} + \frac{\phi\sigma}{U_\infty^2}\right]\mathrm{d}s + \mathcal{O}(\delta^3) \tag{46}$$

The last term is still not a wake integral. To overcome this problem, the work of Cummings et al. [13] can be used [Eq. (22)]. This relation can be applied because Cummings et al. defined their axial velocity variations from a flow without entropy and enthalpy variations. This is the definition of δu^*. As a consequence, this last term is zero to the second order, and the drag expression can be reduced to the wake, with the profile and induced-drag components identified as

$$C_{\text{Dp}}^{\text{ONERA3}} = \frac{1}{S_{\text{ref}}}\int_{\text{wake}}\left[-\frac{2}{\gamma M_\infty^2}\delta P_i - \delta T_i + \left(1-\frac{M_\infty^2}{4}\right)\delta T_i^2 - \delta P_i \delta T_i - \left(1-M_\infty^2\right)(\delta\bar{u}^2 + 2\delta u^*\delta\bar{u})\right]\mathrm{d}s \tag{47}$$

$$C_{\text{Di}}^{\text{ONERA3}} = \frac{1}{S_{\text{ref}}}\int_{\text{wake}}\frac{\psi\zeta}{U_\infty^2}\,\mathrm{d}s \tag{48}$$

With this method, the crossing term $\delta u^*\delta\bar{u}$ is introduced in the profile drag, a point that is arguable. This term represents the interaction of the viscous and wave wakes with the crossflow and could be defined in the profile or in the induced drag. For our applications, this term is very small and its influence on the drag breakdown is negligible. But in the case of slender body or wing flows with separation, crossflow separations will make this term more significant.

Moreover, this new profile drag formulation and the van der Vooren et al. [2,12] formulation are identical to the second order and equal to the asymptotic development of Eq. (33). This confirms that they provide a similar drag breakdown. The only important difference concerns the absence of restriction on the stagnation pressure field for the ONERA3 formulation, which can in turn be applied to compressible flows from a unique experimental wake extraction.

To evaluate the accuracy of this new drag decomposition method, CFD computations were carried out on several configurations (NACA0012 wing, AS28 wing–body, and generic Falcon). Based on these simulations, the different profile drag formulations and axial velocity breakdowns are compared.

IV. Validation of the New Drag-Breakdown Method

A. NACA0012 Rectangular Wing

1. *Computational Method*

Three-dimensional Navier–Stokes computations are carried out with the ONERA-elsA code. The software uses a cell-centered finite volume discretization on structured multiblock meshes. Space discretization is realized through a central scheme with added artificial viscosity. Time integration is carried out using a backward-Euler scheme with implicit lower/upper scalar relaxation. Multigrid methods are used to accelerate convergence. Turbulence effects are modeled using the Spalart–Allmaras one-equation model.

Steady compressible flows around a NACA0012 rectangular with an aspect ratio of 8, in free-air conditions, are simulated. The mesh consists of two blocks of 410,865 nodes (Fig. 10). The computations are carried out for different Mach numbers, from 0.1 to 0.8, for a Reynolds number between 0.5×10^6 and 2.7×10^6, with constant stagnation pressure and temperature. The incidence α is fixed at 2.5 deg. These computations aim at studying and comparing the different profile drag formulations. For this, different wake planes are extracted from the flowfield (Fig. 11). They are located between 0.5 and four chords downstream of the model.

From these simulations, the drag breakdown was also carried out with the $ffd41$ code developed at ONERA [1,14]. This code returns the evaluation of the drag components from Navier–Stokes simulations and is based on the far-field approach with a volume integration of the aerodynamic variables, contrary to the experimental method, which uses a surface integration. This software computes the profile and induced-drag formulations defined by van der Vooren et al. [2,12] (Eqs. (17) and (19). Moreover, this method can correct the downstream numerical diffusion losses

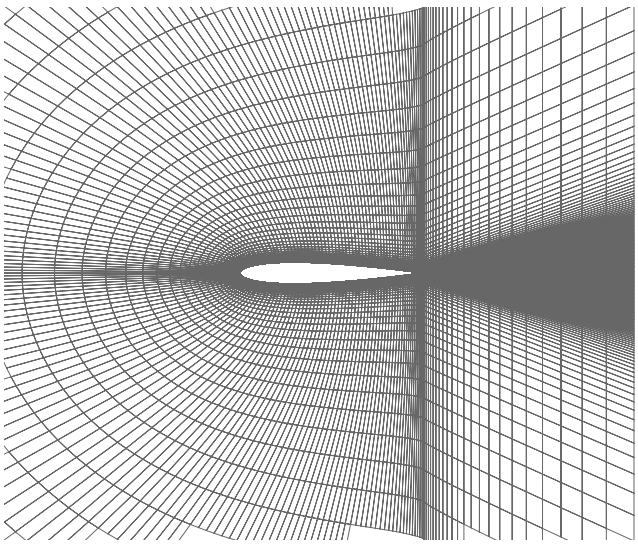

Fig. 10 NACA0012: mesh grid.

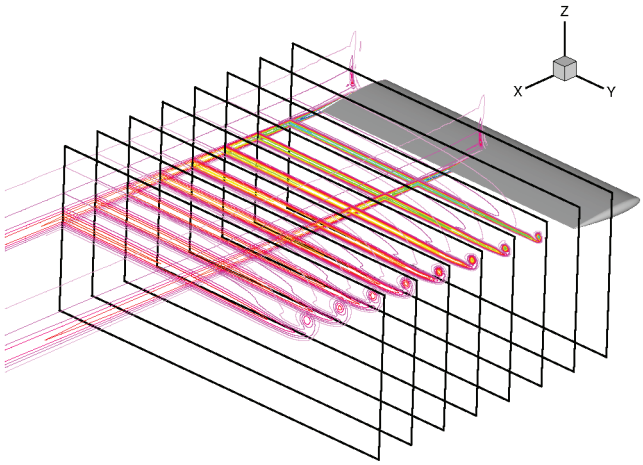

Fig. 11 NACA0012: stagnation pressure field.

by adding them to the induced drag and provides a constant drag breakdown that does not depend on the position of the wake plane downstream of the model. With the experimental method, the downstream numerical diffusion cannot be corrected and the drag values vary along the wake.

Consequently, the experimental method allows a reliable physical drag breakdown only from wind-tunnel measurements. However, numerical computations can be used to determine the reliability of this method. Indeed in each wake plane (Fig. 11), the experimental method can be applied to determine profile and induced drag. These drag components do not correspond with the physical components, because the flowfield in these numerical wake planes is influenced by the numerical diffusion. The application of the experimental method from CFD computations only shows its capability to break down the different physical phenomena that are located in a wake plane. So to have a reliable evaluation of the accuracy of the method, the results have to be compared with those of $ffd41$, but without correction of the numerical diffusion.

It is also important to keep in mind that this study aims at evaluating the accuracy of the experimental method and the ONERA3 formulation from wake data, but it does not aim at evaluating the accuracy of the CFD computations. In these conditions, the grid independence of the numerical model is not of great importance. What is really important is that the comparisons between the experimental and numerical methods always provide similar drag values, even if these values change with the spatial discretization.

These numerical computations were performed to evaluate the capabilities of the experimental method. The numerical method provides accurate results but uses CFD simulations that are affected by numerical errors, whereas the experimental method uses reliable data with unknown accuracy. By comparing both methods on the same flowfield, the capabilities of the experimental method and the ONERA3 formulation can be assessed.

2. *Drag-Extraction Results*

In Figs. 12 and 13, the evolution of profile drag is plotted against the upstream Mach number in the wake plane located at 0.5 chord downstream of the model. From these figures, the accuracy of the experimental method is very convincing indeed, and it provides the same profile drag values as $ffd41$ for the same formulation (van der Vooren et al. [2,12] without correction). From this experimental method, the evolution of the profile drag is evaluated with the different formulations. Figures 12 and 13 show that this evolution is identical for each formulation except for the formulation proposed by Maskell [5]. The difference between this formulation and the others grows quickly with Mach number. This is due to the fact that this formulation is applicable to a compressible flow only if the wake-survey plane is a Trefftz plane, which is rarely the case.

The other formulations have the same behavior, but they do not provide the same profile drag value. They can be classified in five categories: 1) the Maskell [5] formulation (Trefftz assumption); 2) the Oswatitsch [4] formulation; 3) the Betz [11] (Trefftz assumption) and ONERA2 formulations; 4) the Jones [3], van der Vooren et al. [2,12] (Trefftz assumption), and ONERA3 formulations; and 5) the Kusunose [8] and ONERA1 formulations.

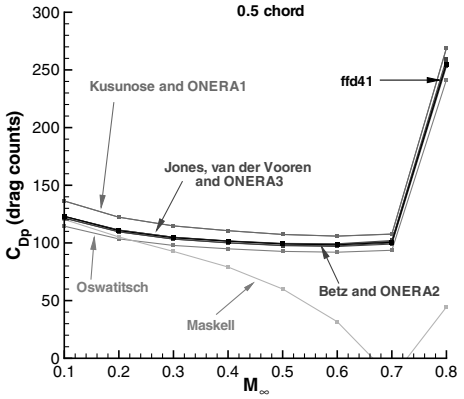

Fig. 12 NACA0012: profile drag at 0.5 chord ($M_\infty = 0.1$ to 0.8).

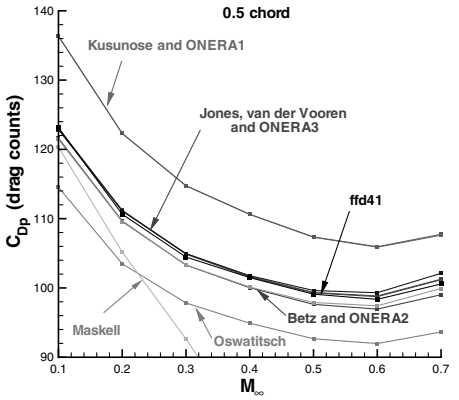

Fig. 13 NACA0012: profile drag at 0.5 chord ($M_\infty = 0.1$ to 0.7).

In each group, the formulations have the same behavior and provide very close profile drag values. These observations are in perfect agreement with the analysis of the asymptotic developments, owing to the fact that in each group, the different expressions are identical to the second order.

The difference between the groups can be quite important. For instance, between the first and the fourth groups, this difference reaches about 20 drag counts for all Mach numbers. This shows the importance of the formulation and of the axial velocity field to reach an accurate phenomenological drag breakdown. Indeed, the second group takes into account all these velocity variations in the profile drag, contrary to the fourth group, which only considers the stagnation pressure and temperature losses. The third group is an alternative to the second group, due to its physical breakdown of the axial velocity. The Oswatitsch [4] formulation underestimates the profile drag, because the second-order terms are neglected in Eq. (11).

The comparison between the van der Vooren et al. [2,12] and the ONERA3 formulations shows very close results, especially in subsonic conditions. In transonic flows, a slight difference between both formulations appears and increases with the Mach number. This difference is due to the small-disturbance assumption, which is invalid at these conditions in which the stagnation pressure losses become too important (20%). Nevertheless, this difference remains lower than one drag count in all configurations.

Figure 14 shows the evolution of the formulations in different wake planes. For the formulations of the first two groups, the profile drag increases slightly with the distance between the wake plane and the model; for the fourth group, the profile drag decreases; and for the third group, the profile drag remains constant.

From the plane located at one chord downstream of the model, the difference between the formulations of the second and third groups becomes very small. The variations of static pressure and axial velocity δu^* fields decrease quickly and their influence on the profile drag eventually becomes very small. For the fourth group, the difference remains important when compared with the others, even if it decreases along the wake (three drag counts at four chords). This difference is due to the variations of the viscous axial velocity field, which remain important far downstream of the wing. In the far field, all formulations converge toward a single value.

The Maskell [5] formulation provides very poor results in the first wake plane, even at subsonic conditions ($M_\infty = 0.2$). When the position of this plane changes, the behavior of the formulation improves. Indeed, in the wake plane located at four chords downstream of the model, the formulation provides reliable results up to a Mach number of 0.3.

The slight difference that appears in the first wake plane between the van der Vooren et al. [2,12] and the ONERA formulations in transonic conditions decreases when the wake plane moves away from the wing. This evolution is linked to the diffusion of the

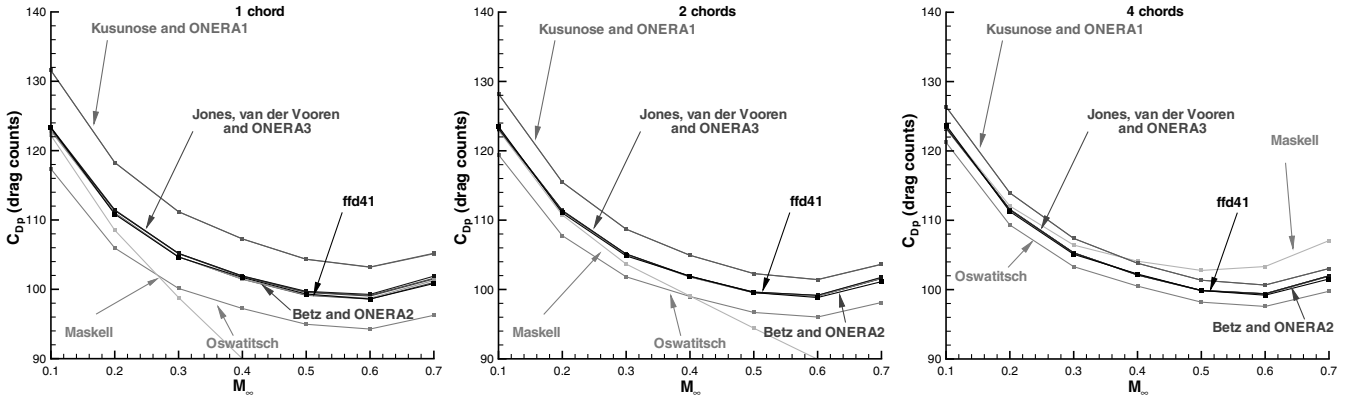

Fig. 14 NACA0012: profile drag.

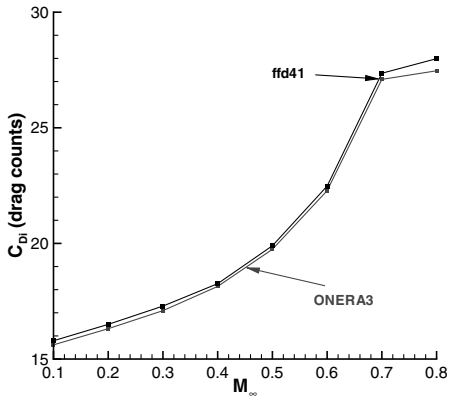

Fig. 15 NACA0012: induced drag at 0.5 chord ($M_\infty = 0.1$ to 0.8).

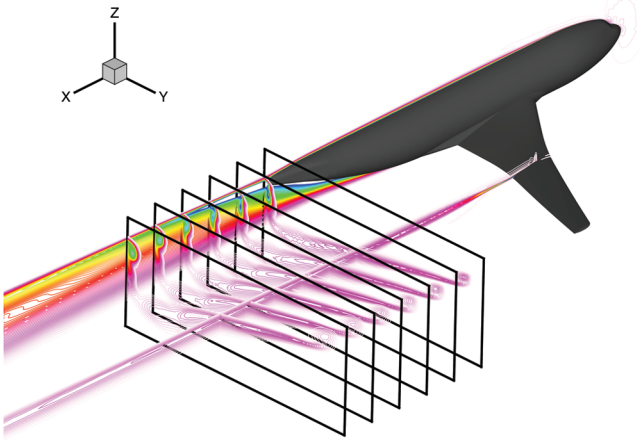

M_∞=0.8 - α=1.62^0

Fig. 16 AS28: stagnation pressure field.

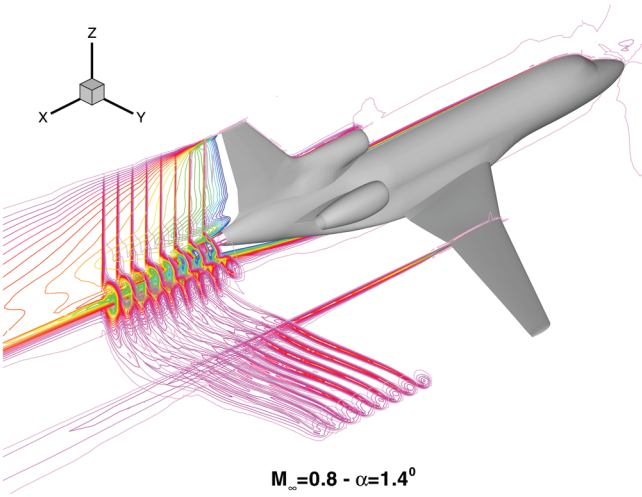

M_∞=0.8 - α=1.4^0

Fig. 17 Generic Falcon: stagnation pressure field.

stagnation pressure losses, in which the small-disturbance assumption becomes perfectly licit in these far wake planes. Figure 15 shows the evolution of the induced drag with the Mach number in the first wake plane. Both curves correspond to the results obtained with $ffd41$ (without numerical and physical corrections and using the van der Vooren et al. formulation) and the experimental drag-extraction method (the ONERA3 formulation), respectively. Both methods provide similar values, the difference remaining lower than one drag count for all Mach numbers.

To summarize, this first numerical study clearly underlines the importance of the axial velocity on the drag breakdown. To obtain an accurate phenomenological breakdown, the axial velocity variations have to be divided into two components. Moreover, this study shows the accuracy of the experimental drag-extraction method associated with the new ONERA3 formulation. To validate the method for a more complex case, similar computations were conducted on the AS28 wing–body and generic Falcon configurations in the following section. The generic Falcon configuration consists of a fuselage, a wing, three throughflow nacelles, and a vertical stabilizer.

B. AS28 Wing–Body and Generic Falcon

1. *Computational Method*

For the AS28 wing–body configuration, the three-dimensional Navier–Stokes computations were carried out with the same numerical parameters as for the previous configuration. For the generic Falcon configuration, the turbulence model used for the computations is the two-equation k–ω of Wilcox. For both configurations, the simulations are realized for steady compressible flows in free-air conditions, for different Mach numbers, from 0.1 to 0.85, and Reynolds numbers between 8×10^5 and 2.6×10^6. The incidence α is fixed at 1.62 deg for the AS28 configuration and 1.4 deg for the generic Falcon configuration. The mesh is made up of 48 blocks and 6,743,920 nodes in the first case and 92 blocks and 7,702,402 nodes for the second case. These computations aim at studying and comparing different profile drag formulations in a complex configuration to validate the experimental drag-extraction method and the ONERA3 formulation. For this, different wake planes are extracted from the flowfield (Figs. 16 and 17). They are located between 0.5 and two chords downstream of the model.

2. *Drag-Extraction Results*

As for the NACA0012 wing configuration, all the profile drag formulations were computed in each wake plane for the each different simulation. For both configurations, the drag-extraction

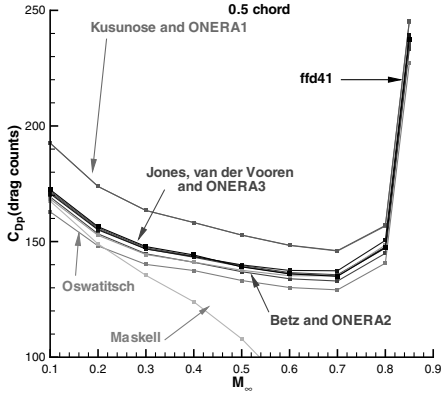

Fig. 18 AS28 wing–body: profile drag at 0.5 chord ($M_\infty = 0.1$ to 0.85).

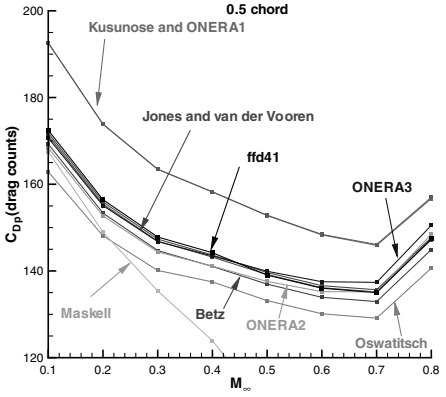

Fig. 19 AS28 wing–body: profile drag at 0.5 chord ($M_\infty = 0.1$ to 0.8).

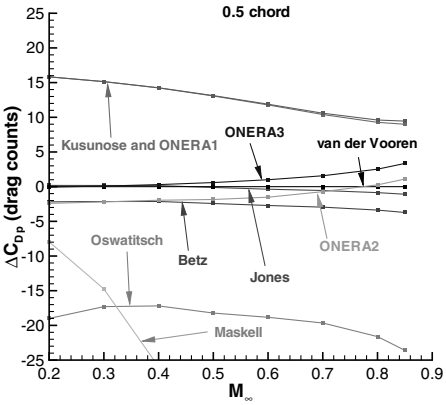

Fig. 20 Generic Falcon: profile drag at 0.5 chord ($M_\infty = 0.1$ to 0.85).

method shows very convincing results, with a difference (between this method and $ffd41$) lower than one drag count for all Mach numbers using the van der Vooren et al. [2,12] formulation. In Figs. 18–20, the results are plotted for the first wake plane, located 0.5 chord downstream of the configurations. For the generic Falcon, these results are presented in terms of the difference with the van der Vooren formulation, which is used as a reference. In this figure, the different curves have the same behavior as for the previous configuration, and the formulations can be classified in the same four categories.

In addition, Figs. 19 and 20 show the influence of the small-disturbance assumption on the results. At low Mach numbers, the formulations, which have the same asymptotic development, provide the same profile drag values; but for Mach numbers up to 0.5, the difference between the small-disturbance-assumption-based expressions and the others grows. This appears between the Betz [11] and the ONERA2 formulations and between the van der Vooren et al. [2,12] and the ONERA3 formulations. This phenomenon is due to the fact that the small-disturbance assumption is violated when the stagnation pressure losses become significant. The error, in term of drag, can reach up to 2.5 drag counts for the generic Falcon configuration at a Mach number of 0.85.

Figures 21 and 22 show the evolution of the different formulations in different wake planes for both configurations. All formulations converge toward a single value in the far field. Moreover, the influence of the small-disturbance assumption becomes negligible on these wake planes, because the stagnation pressure losses decrease along the wake. These computations on complex configurations confirm the results of the first study and the importance of the axial velocity breakdown on the evaluation of the different drag components.

Finally, these numerical studies show the capabilities of the experimental drag-extraction method associated with the new ONERA3 formulation to provide an accurate phenomenological drag breakdown from a rigorous analysis of the drag sources. This method can be applied in wind-tunnel tests in subsonic and transonic flows to evaluate the influence of a given aerodynamic element on the different drag components.

V. Applications

A. Wake and Balance Measurements

To evaluate the precision of the new drag-extraction method from wind-tunnel measurements, the results have to be compared with a reference value. This comparison can be carried out with balance measurements, which provide a reliable evaluation of the total drag.

In the wind tunnel, the upstream flow conditions do not correspond to the flow conditions around the model. Indeed, the presence of walls and various elements inside the tunnel significantly modifies the flow properties. The upstream conditions are imposed so that the flow around the model corresponds to the chosen aerodynamic conditions: free air, in flight quantities. To account for that, corrections translating compressibility and blockage confine-

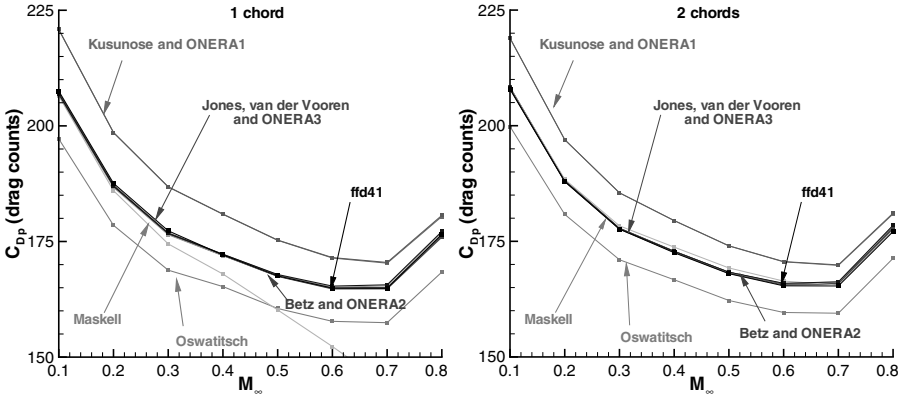

Fig. 21 AS28 wing–body: profile drag.

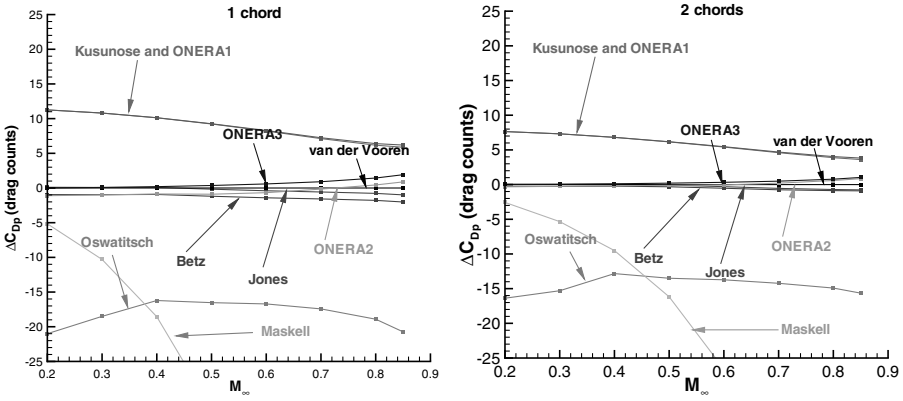

Fig. 22 Generic Falcon: profile drag.

ment effects are therefore applied to Mach number, incidence, and lift and drag.

To evaluate the reliability of the new drag-extraction method, it is important to know if wake measurements have to be compared with corrected or uncorrected balance values. In the wake plane, the flow conditions correspond to the corrected values in terms of Mach number and incidence. However, the confinement effects cannot be directly corrected. As a consequence, the different variables measured in the flowfield are affected by these effects. Their influence on the wake variables (stagnation values) is negligible, but is very important on the others, especially on crossflow velocities.

In the new ONERA3 formulation, the profile drag is mainly computed from wake variables and, as such, it is not affected by these confinement effects. On the contrary, the induced drag is exclusively computed from the crossflow velocities. They are used to determine the axial vorticity field and the streamline function [Eq. (48)]. However, contrary to the crossflow velocity field, the local vorticity is zero outside the wake and so is not really affected by confinement effects. Furthermore, if the wake plane is located less than five chords downstream of the model, this vorticity field can be considered equivalent to a free-air vorticity field obtained with the same aerodynamic conditions, but without walls [7]. Concerning the streamline function, it is computed from this vorticity field using the following equation: $\Delta\psi = -\zeta$. To solve this equation, free-air boundary conditions can be imposed to determine a free-air streamline function.

Using the ONERA3 formulation, the induced drag is thus computed from a confined vorticity field, which is equivalent to the free-air vorticity field, and from a free-air streamline function; as a consequence, it corresponds to the free-air induced drag. Moreover, the profile drag computed with this formulation also corresponds to a free-air value. In conclusion, the total drag computed from wake measurements should be compared with the corrected balance value.

B. Data Reduction and Correction

The data-reduction procedure used in the current analysis consists in the interpolation of the measured data on computational Cartesian grid points and a correction of the normalized stagnation pressure.

Interpolation of the measured variables is performed using a linear or a cubic spline scheme. The latter is used if the measured data point's location is not homogeneous in the wake-survey plane. To obtain accurate results, wake surveys not only require a large number of data points, but also very accurate probe-position measurement, because spatial derivatives of flow velocities must be computed. Indeed, the induced drag requires the crossflow velocity components to be numerically differentiated, using a central-difference scheme.

Although the noise level is low, the correction of the stagnation pressure is essential. The normalized stagnation pressure Pi/Pi_∞ is shifted exactly to one outside the wake.

C. Subsonic Tests

In this section, an application is presented that aims at determining the influence of a nacelle on a high-lift configuration. It consists of a fuselage and a wing equipped with high-lift elements (flaps, slats, and fairings). These tests aimed at evaluating the influence of a throughflow nacelle on the viscous C_{Dv} and induced-drag C_{Di} components. Within the framework of the EUROLIFT2 European project, they were carried out at the Airbus Deutschland low-speed wind tunnel of Bremen on the half-model KH3Y (Fig. 23) in landing configuration at a Mach number of 0.174. The test section is 2.1 m (6.9 ft) high, 2.1 m (6.9 ft) wide, and 4.3 m (14.1 ft) long. The five-hole-probe measurements were performed on the two configurations, with and without a nacelle. The measuring plane was located near the rear of the fuselage. Balance measurements were also carried out to compare the results in terms of total drag.

Figures 24 and 25 show the local and spanwise viscous and induced-drag distributions for both configurations. The local fields allow a very detailed study of the drag sources. In both configurations, the main viscous sources are located downstream of the wing tip vortex and the fuselage. Several other sources appear downstream of the different high-lift elements and the nacelle. In the spanwise distributions, these sources can be identified and the strong

Fig. 23 Half-model KH3Y.

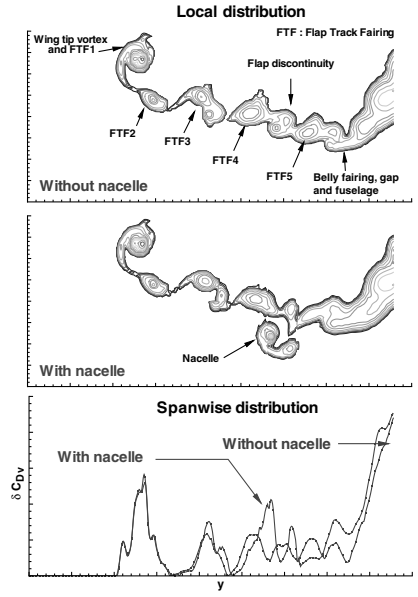

Fig. 24 Profile drag.

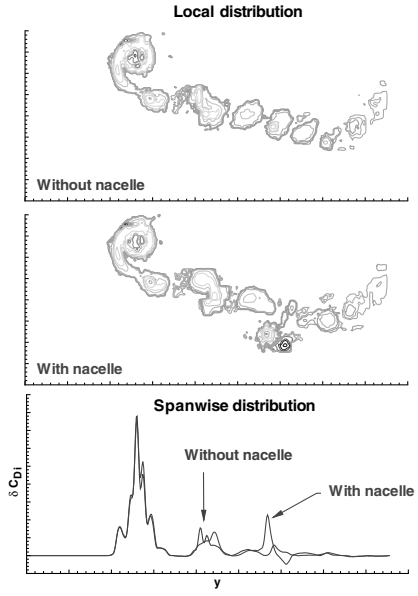

Fig. 25 Induced drag.

influence of the nacelle is observed on the inboard wing. This influence is not only strong on the viscous drag, but also on the induced component, due to the lift increase.

Table 1 shows the results of the drag-extraction method and the differences between both configurations. The different formulations provide varying ΔC_{Dp} values, but again, groups of identical (or similar) to those found during the numerical data analysis can be constructed. The comparison between balance ($\Delta C_D = 170$) and wake surveys shows a good coherence for total drag, but a slight difference for lift. The latter is slightly underestimated by the ONERA3 formulation.

Table 1 Influence of the nacelle on the drag components: $\Delta C_D \equiv C_D^{\text{with nacelle}} - \Delta C_D^{\text{without nacelle}}$

	ΔC_L	ΔC_D(dc)	ΔC_{Dp}(dc)	ΔC_{Di}(dc)
Balance measurements	0.02	170		
Wake measurements				
Betz [11]	0.06		64	
ONERA2	0.06	169	64	105
Jones [3]	0.06		69	
Van der Vooren et al. [2,12]	0.06		70	
ONERA3	0.06	162	71	91
Kusunose [8]	0.06	170	79	91
ONERA1	0.06	169	79	90

Table 2 Comparison with ONERA3 formulation: $\delta C_D \equiv C_D - C_D^{\text{ONERA3}}$

	δC_{Dp}(dc)	
	No nacelle	Nacelle
ONERA2	7.5	14.0
Van der Vooren et al. [2,12]	0.4	2.7
Kusunose [8]	43.0	57.1

Table 2 shows a comparison for each configuration of the formulations against an ONERA3 reference. The van der Vooren formulation provides a similar decomposition, because it belongs to the same group. The differences with the ONERA2 formulation correspond to those of Table 1 (7(dc) $\sim 169 - 162 \sim 14 - 7.5$). On the other hand, the Kusunose [8] formulation provides much greater values, a result that is in agreement with the numerical data analysis. This formulation overestimates the total drag of each configuration, but with a constant offset, so that the difference between them is well-predicted. We can thus conclude that the more accurate formulations (for profile drag) are the van der Vooren et al. [2,12], ONERA2, and ONERA3 formulations.

This study proves the reliability of the new formulation for evaluating the different drag components. Indeed, all formulations provide good results for the influence of the nacelle, whereas the ONERA3 formulation allows a more accurate prediction of the absolute drag values in both configurations. Moreover, in the measuring plane, the limitation imposed by the van der Vooren et al. [2,12] formulation on the stagnation pressure losses is reached in the core of the wing tip vortex. In these conditions, this last formulation is not able to provide an accurate axial velocity and drag breakdown, whereas the ONERA3 formulation is not affected.

D. Nacelle Effects in Transonic Flow

Tests were conducted in the ONERA-S2MA wind tunnel on a full model to determine the influence of a nacelle in a transonic flow close to cruise conditions. The S2MA wind tunnel is of the continuous-flow pressurized type, fitted with two interchangeable test sections for transonic and supersonic operation. The transonic test section (for Mach 0.1 to 1.3) with perforated walls is 1.77 m (5.8 ft) high, 1.75 m (5.74 ft) wide, and 3.75 m (12.3 ft) long. The stagnation pressure can be varied up to 2.5 bar. The wake-survey device (six degrees of freedom) is composed of different elements that can rotate independently, in addition to providing translation. At the upstream extremity of the device is a sting 1.0 m (3.28 ft) long, supporting one five-hole probe. The wake measurements are performed in a plane downstream of the model, by vertical displacements of the probe at different lateral positions. The vertical velocity of the probe is generally 5 mm/s (0.197 in./s), with a measurement point approximately 0.5 mm (0.02 in.) [15].

Balance and wake measurements were carried out on two configurations, with and without nacelles, for two lift values ($C_{L1} < C_{L2}$). Figures 26 and 27 show the local and spanwise profile drag distributions for both configurations and lift values. For the configuration without a nacelle, the viscous wake is slightly affected by the lift variation, whereas the shock becomes stronger and spreads on the whole wingspan for the highest lift value. The comparison between the configurations with and without nacelles highlights its influence on the viscous and wave wakes. The spanwise distributions show that the nacelle does not modify the whole wake but is only responsible for an additional profile drag source.

For the transonic case, Table 3 only displays the profile drag differences for each formulation and for the two lift values. We note a similar precision, with the maximum difference between two formulations less than two drag counts. As in the subsonic case,

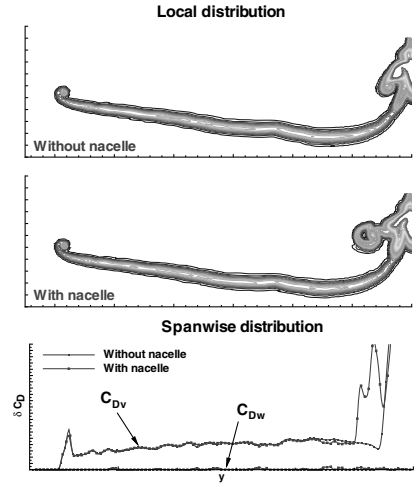

Fig. 26 Profile drag (C_{L1}).

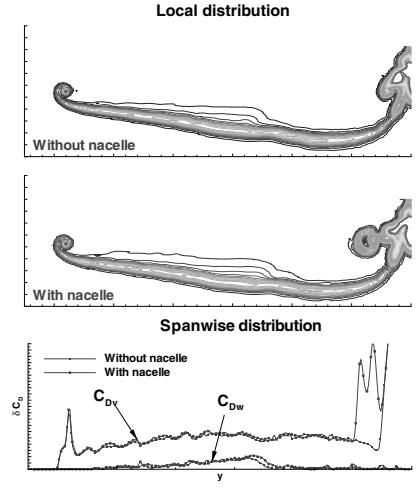

Fig. 27 Profile drag (C_{L2}).

Table 4 compares the most interesting formulations against ONERA3. The differences are twice as large for the Kusunose [8] formulation than they are for the van der Vooren et al. [2,12] and ONERA2 formulations. It seems that for transonic flows with shocks, the formulations provide results with the same accuracy. This point is in agreement with the results from numerical data analysis, as displayed in the Fig. 12.

It is important to compare these results with the balance measurements. Table 5 displays the differences between ONERA3 and balance total drag values. The maximum difference reaches up to 3.5 drag counts, on the same order of magnitude as the differences between two formulations.

Throughout this application, the reliability of the drag-extraction method from wake measurements was demonstrated in transonic flow. Furthermore, the drag breakdown allowed an accurate analysis of the different drag sources generated by a given aerodynamic element, a throughflow nacelle, in this case.

Table 3 Influence of nacelle on the drag components: $\Delta C_D \equiv C_D^{\text{with nacelle}} - \Delta C_D^{\text{without nacelle}}$

	ΔC_{Dp}(dc)	
	CL1	CL2
Betz [11]	20.2	27.4
ONERA2	20.4	28.0
Jones [3]	20.1	27.3
Van der Vooren et al. [2,12]	20.2	27.5
ONERA3	21.5	27.8
Kusunose [8]	21.3	28.9
ONERA1	21.4	28.9

Table 4 Comparison with ONERA3 formulation: $\delta C_D \equiv C_D - C_D^{\text{ONERA3}}$

		δC_{Dp}(dc)	
		No nacelle	Nacelle
Kusunose [8]	CL1	5.2	6.0
	CL2	5.3	6.4
Van der Vooren et al. [2,12]	CL1	2.2	2.5
	CL2	2.3	2.6
ONERA2	CL1	2.5	2.6
	CL2	2.6	2.4

Table 5 Influence of nacelle on the drag components in transonic flow: ONERA3 formulation

C_L	$C_D^{\text{wake}} - C_D^{\text{balance}}$(dc)	
	No nacelle	Nacelle
C_{L1}	0.6	3.5
C_{L2}	1.3	0.4

VI. Conclusions

To carry out an accurate phenomenological drag breakdown, different profile and induced-drag definitions were analyzed to determine their influence on the decomposition on one hand and their physical meaning on the other hand. This study underlined the importance of the axial velocity and static pressure fields. Some formulations provided an accurate phenomenological breakdown, but could not be applied to all configurations. To overcome this difficulty, a new drag-breakdown method was developed. A numerical study on a NACA0012 rectangular wing, a AS28 wing–body, and a generic Falcon configuration demonstrated the accuracy of the new method. Very convincing results were obtained through a comparison with a three-dimensional drag-extraction code ($ffd41$).

This experimental method was applied to wind-tunnel measurements in subsonic and transonic conditions. These studies underlined the capabilities of the new drag-extraction method to evaluate the influence of nacelles on the different drag components with a good accuracy. The difference with the other formulations was very low in terms of relative drag values, but quite important for the absolute values: specifically, for the high-lift configuration. Consequently, this new drag-breakdown method provided results in closer agreement to the balance measurements when compared with the others, especially for subsonic and free-shock transonic flows. Furthermore, the breakdown of the profile drag into viscous and wave components can be carried out using an original method developed at ONERA and is compatible with any profile drag formulations.

Acknowledgment

The authors want to express their thanks to Stephen MacParlin for his constructive contribution, which led us to write this paper in its present form.

References

[1] Destarac, D., "Far-Field/Near-Field Drag Balance and Applications of Drag Extraction in CFD," *CFD-Based Aircraft Drag Prediction and Reduction*, VKI Lecture Series 2003, 2nd ed., von Kármán Inst. for Fluid Dynamics, Rhode-Saint-Genèse, Belgium, 2003.

[2] Van der Vooren, J., and Destarac, D., "Drag/Thrust Analysis of Jet-Propelled Transonic Transport Aircraft; Definition of Physical Drag Components," *Aerospace Science and Technology*, Vol. 8, No. 6, 2004,

pp. 545–556.
doi:10.1016/j.ast.2004.03.004
[3] Jones, B., "Measurement of Profile Drag by the Pitot-Traverse Method," Aeronautical Research Council, Reports and Memoranda No. 1688, 1936.
[4] Oswatitsch, K., *Gas Dynamics*, Academic Press, New York, 1956.
[5] Maskell, E. C., "Progress Towards a Method of Measurement of the Components of the Drag of a Wing of Finite Span," Royal Aircraft Establishment TR 72232, Jan. 1973.
[6] Bailly, D., and Godard, J., "Méthodologie Expérimentale pour l'évaluation de la Traînée, Techniques de Post-Traitement, Préparation d'essais," ONERA RT 116/1685 DAAP/Y, 1999.
[7] Méheut, M., and Bailly, D., "Drag Prediction and Wake Survey Techniques," *CEAS/KATnet Conference on Key Aerodynamic Technologies* [CD-ROM], Conference Data Services, Hampshire, England, U.K., 20–22 June 2005.
[8] Kusunose, K., *A Wake Integration Method for Airplane Drag Prediction*, Tohoku Univ. Press, Sendai, Japan, 2005.
[9] Van Dam, C., "Recent Experience with Different Methods of Drag Prediction," *Progress in Aerospace Sciences*, Vol. 35, No. 8, 1999, pp. 751–798.
doi:10.1016/S0376-0421(99)00009-3
[10] Chao, D., and van Dam, C., "Airfoil Drag Prediction and Decomposition," AIAA Paper 98-2783, 1998.
[11] Betz, A., "A Method for the Direct Determination of Wing-Section Drag," *Zeitschrift für Flugtechnik und Motorluftschiffahrt*, Vol. 6, 1925, pp. 42.
[12] van der Vooren, J., and Slooff, J., "CFD-Based Drag Prediction; State-of-Art, Theory, Prospects," National Aerospace Lab., NLR, TP 90247 U, 1990.
[13] Cummings, R., Giles, M., and Shrinivas, G., "Analysis of the Elements of Drag in Three-Dimensional Viscous and Inviscid Flows," AIAA Paper 96-2482, 1996.
[14] Esquieu, S., "Evaluation de la Traînée d'un Avion De Transport à Partir de Calculs Numériques de Mécanique des Fluides," Ph.D., Thesis, Univ. de Bordeaux, Bordeaux, France, 2003.
[15] Sechaud, J-F., Wolf, S. W. D., Carraz, G., Raynal, J-C., Godard, J-L., Bailly, D., and Coton, P., "Wake Survey Techniques in the ONERA Industrial Wind Tunnels," 22nd AIAA Aerodynamic Measurement Technology and Ground Testing Conference, AIAA Paper 2002-2923, 24–26 June 2002.